



Modelling pellet size and shape evolution during the breakage stage in spheronisation

J. Whelan-Smith^a, M.S. How^b, S.L. Rough^a, L. Wang^c, D.I. Wilson^{a,*}

^a Department of Chemical Engineering and Biotechnology, University of Cambridge, Philippa Fawcett Drive, Cambridge CB3 0AS, UK

^b Department of Process and Food Engineering, Faculty of Engineering, Universiti Putra Malaysia, Serdang 43400, Malaysia

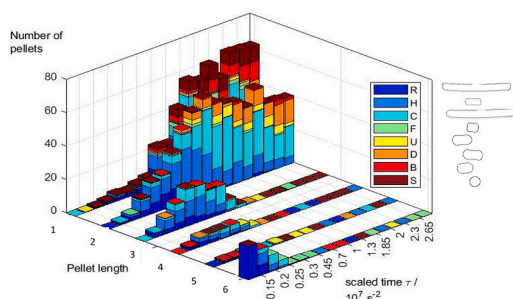
^c School of Chemical Engineering, The University of Queensland, Brisbane, Queensland 4072, Australia

HIGHLIGHTS

- Pellet length (6 classes) and shape (8 categories) were identified from >17,000 images.
- Breakage and rounding occur simultaneously, with rounding dominant for $L/D < 3$.
- A 2-dimensional population balance model is presented which captures the trends.
- Better agreement requires better, automated, image classification methods.

GRAPHICAL ABSTRACT

Modelling pellet size and shape evolution during the breakage stage in spheronisation



ARTICLE INFO

Keywords:

Extrusion-spheronisation
Microcrystalline cellulose
Pellet shape
Rounding

ABSTRACT

In the breakage stage of extrusion-spheronisation, initially cylindrical extrudates undergo simultaneous breakage and rounding on a rotating friction plate. This sets the starting conditions (number of pellets, size and shape distributions) for the subsequent, lengthy, rounding stage. The simultaneous evolution of pellet size and shape during the initial stages of spheronisation has not been considered in depth. Wang et al. (2021) *AIChEJ*, 67(6), e17247 investigated the breakage of 2 mm diameter microcrystalline cellulose/water extrudates and modelled the evolution of length using a 1-D population balance model. Here the data (over 17,000 images) were re-analysed and classified by both length and shape (8 shape classes). Their model was extended to 2-D (tracking size and shape), and the data fitted by a combination of optimization approaches. The effect of pellet length on the likelihood of breakage over rounding, and the influence of plate rotation speed and initial number of extrudates, is reported.

* Corresponding author.

E-mail address: diw11@cam.ac.uk (D.I. Wilson).

<https://doi.org/10.1016/j.powtec.2024.119465>

Received 29 November 2023; Received in revised form 21 January 2024; Accepted 24 January 2024

Available online 28 January 2024

0032-5910/© 2024 The Author(s). Published by Elsevier B.V. This is an open access article under the CC BY license (<http://creativecommons.org/licenses/by/4.0/>).

Nomenclature	
<i>Roman</i>	
A_{proj}	Projected area, m ²
AR, AR_0, AR_{fin}	Aspect ratio, initial value, final value, –
b_i	Sum of breakage rate constants for pellets of length i s ²
$B_{i,jD}$	Net breakage rate for pellets of length $I, j = 1D$ or $2D, s^2$
d_p	Spheroniser plate diameter, m
D	Extrudate diameter, m
$k_{1,j,i-j}$	Breakage kinetic constant, 1-D model, s ²
$k_{1s1,js2,ks3}$	Breakage kinetic constant, 2-D model: i, j, k indicate length of pellets; $s1, s2, s3$ indicate shape, s ²
k_r	Rate constant, Eq. (1), s ⁻¹
$k_{1s1,js2}$	Rounding kinetic constant, 2-D model, s ²
L_0	Initial rod length, m
L	Extrudate length, m
n_i	Number of pellets of length i at time τ , –
$n_{i,s}$	Number of pellets of length i and shape s at time τ , –
N_{all}	Total number of pellet images studied, all interval, s–
N, N_0, N_{fin}	Total number of pellets at given time, initial value, final value, –
P	Perimeter length, m
$p_{B,i}$	Net likelihood of breakage, –
R_i	Sum of rounding rate constants for pellets of length i, s^2
R^2	Coefficient of determination, –
r_p	Radius of spheroniser friction plate, m
s	Label for shape of pellet (see Table 2), –
t	Time, s
W	Pellet width, m
<i>Greek</i>	
χ	Circularity: R – rod; C – cigar; H – half-cigar, –
μ_i	Mean of the number of pellets of classification i at time τ , –
σ_i	Standard deviation of the number of pellets of classification i at time τ , –
τ	Scaled time, s ⁻²
ω	Spheroniser rotational speed, s ⁻¹
<i>Acronyms</i>	
BCA	Boundary constraint algorithm
DEM	Discrete element modelling
E-S	Extrusion-spheronisation
GA	Genetic algorithm
GD	Gradient descent
MCC	Microcrystalline cellulose
ODE	Ordinary differential equation
PBM	Population balance model
PSO	Particle swarm optimisation

1. Introduction

Extrusion-spheronisation (E-S) is a granulation method that yields pellets with high density and sphericity [1,2]. The particulate solids are firstly combined with a liquid (the binder) to give a dense wet mass (also termed ‘dough’ or ‘paste’) which is then ram-, screw- or screen-extruded through circular holes (often several in number) to give cylindrical extrudates of random length but uniform diameter, D . The extrudates are then spheronised on a rotating friction plate which features protuberance patterns that (i) promote the breakage of the extrudates and (ii) drive the formation of a toroidal bed in which the shorter fragments (here termed pellets) are subject to multiple collisions in a complex motion (see e.g. [3,4]).

Studies of spheronisation dynamics, e.g. [5,6], have shown that spheronisation is a two-stage process. In the first stage, collisions between the cylindrical rod-shaped extrudates and the wall, the friction plate, and other extrudates result in *breakage*, forming two or more rods of shorter length. The rod length L is conveniently quantified as the pellet aspect ratio, $AR = L/D$. As the number of pellets increases and rod length decreases, collisions are less likely to cause breakage and instead result in plastic deformation, promoting *rounding* (the second stage). The number of pellets does not change significantly in this stage and the rounding of short rods has been modelled in detail using numerical methods such as DEM, e.g. [4,7,8]. Breakage of rods in agitated beds, e.g. [9], has been modelled using these methods, but simulating the initial breakage stage in spheronisation has not been attempted, partly because the starting condition varies widely in that the extrudate lengths are not controlled.

The importance of the breakage stage lies in it setting the starting conditions (number of pellets, N , size and shape distributions) for the subsequent rounding stage. Studies of spheronisation dynamics (e.g. [10,11]) have reported that the evolution of pellet shape, often quantified by an average aspect ratio, AR , during the rounding stage follows the relationship

$$AR(t) = AR_{fin} + (AR_0 - AR_{fin})exp(-k_r t) \quad (1)$$

where AR_0 and AR_{fin} are the initial and final values of the aspect ratio,

respectively (an AR value of 1.2 is often cited as acceptable for subsequent process operations as tableting or capsule filling); t is time and k_r is a kinetic constant. Evers et al. [11] investigated the effect of initial loading and plate diameter, d_p (0.12, 0.25 and 0.38 m) on k_r , AR_0 and AR_{fin} for 1 mm diameter extrudates. They reported size and shape data after 30 s and reported initial (AR_0) values in the range 1.4–2.4 and AR_{fin} values of 1.05–1.25, confirming that breakage was mostly complete by the time they started sampling.

For a given load of extrudates the timescale of breakage and of rounding (i.e. k_r^{-1}) is expected to depend on the rotational speed, ω . Parkin et al.’s dimensional analysis [10] gave a scaled time $\tau = \omega^3 t$ which mapped data sets for rounding conducted at different speeds using a given plate (protuberance pattern, diameter) on to a common trend. Wang et al. [12] conducted a detailed analysis of the breakage stage for $D = 2$ mm extrudates of a model pharmaceutical paste (45 wt% microcrystalline cellulose, MCC, and water) on a $d_p = 0.12$ m friction plate, interrupting the tests at regular intervals to track the change in pellet size and number. They employed initial loadings of 20 or 80 identical extrudates ($AR = L/D = 10$) and found that scaling the time as $\tau = \omega^3 t$ again collapsed the breakage data on to a common trend. Little further breakage occurred after $\tau \sim 2 \times 10^7$ s⁻². This is comparable with the results reported by Evers et al., where the first samples at low speed for their $d_p = 0.12$ m plate, corresponding to $\tau = 0.7 \times 10^7$ s⁻², featured $AR_0 \sim 2$. It should be noted that Evers et al. [1] employed higher loadings, which they reported as (mass of extrudates)/ d_p^3 , with values of 16–100 kg m⁻³; the tests in [12], with 20 and 80 extrudates, featured loadings of 0.73 and 2.9 kg m⁻³, respectively.

Wang et al. presented a simple population balance model (PBM) to describe the evolution of pellet size, $n_i(\tau)$, where n_i is the number of pellets in size range i . Image analysis of each pellet yielded its aspect ratio: the values ranged from 1.3 to ~ 10 so they allocated each pellet to one of 6 bins of width 10/6, i.e. $i = 1, AR < 1.66; i = 2, 1.66 \leq AR < 3.3$, etc. They described breakage as a set of first-order events (see Supplementary Material S1) in which pellets with $i \geq 2$ were assumed to yield two smaller pellets on breakage, of bin sizes j and k where $i = j + k$ and i, j and k are all integers. Mass loss during collisions and attrition was ignored. Table 1 summarises the experimental conditions that they

Table 1

Operating conditions in Wang et al. studies [12]. N_{fin} is the number of pellets at the end of the test, where $\tau = 3.5 \times 10^7 \text{ s}^{-2}$.

Case	ω /rpm	Rim speed / m s^{-1}	N_0 /–	N_{fin} /–	Repeats
I	288	1.81	20	110.3 ± 7.4	4
II	431	2.71	20	119.7 ± 1.2	4
IIIa	575	3.61	20	104.6 ± 5.4	5
IIIb	575	3.61	80	355 ± 16	4
IV	1150	7.23	20	109.7 ± 3.3	3

studied. Their population balance model featured six ordinary differential equations (ODEs) and they estimated the constants for each Case by optimising the least-squares fit in Microsoft Excel.

Wang et al. observed noticeable changes in pellet shape during the breakage stage in their tests, conducted with initially identical rods. They did not include any effect of shape in their breakage model. Lau et al. [5] and Bryan et al. [6] also reported changes in pellet shape at the early stage of spheronisation, indicating that rounding and breakage occur simultaneously: we postulate that some shapes undergo rounding rather than break as a result of a collision, which will in turn determine the duration of the breakage stage (in which most collisions result in a change of number of pellets) as well as the resulting AR distribution. This paper reanalyses sets of the images collected by Wang et al. to determine the evolution of size and shape during the breakage stage and thereby provide insights into breakage mechanisms which could be employed to tailor the speed or protuberance pattern to optimise the (n_i , AR_{fin}) distribution for subsequent rounding. Zhang et al. [13] investigated the effect of protuberance geometry on final pellet shape, and their work could be extended to the breakage stage using the methods presented here.

A two-dimensional population balance model (PBM) is thus presented here, quantifying the evolution of size and shape, extending the kinetic scheme of Wang et al. To the authors' knowledge this has not been attempted previously.

1.1. Pellet shape and characterisation

The experimental protocols used to generate extrudates were reported in [12]. In short, MCC-water paste was ram-extruded through a 2 mm diameter 316 stainless steel die and the cylindrical extrudates promptly cut to a common initial length, $L_0 = 20 \text{ mm}$ (giving $AR_0 = L_0/D = 10$). The desired number, N_0 , was loaded into a Caleva 120 Spheroniser (see Fig. 1) fitted with a 120 mm 316 stainless steel friction plate and spheronised at constant speed for a set time. The pellets were then either removed and photographed, or photographed in situ before restarting the spheroniser. Both methods gave compatible results. ImageJ (National Institutes of Health, USA) was used to determine the length L , width W , AR and circularity χ ($\chi \equiv 4\pi A_{\text{proj}}/P^2$, where P is the perimeter length) of each pellet.

Visual inspection was used to assign pellets into the eight shape categories shown in Table 2 on the basis of the shape of each end. This required analysis of 17,666 pellets and was subject to cross-checking for a sub-set of images. Some pellets did not lend themselves readily to classification, either because of their irregular shape, roughness (both being exacerbated by fines adhering to the surface) or bending: automation of this task using deterministic and machine learning approaches is the subject of a separate paper (manuscript in preparation). Fig. 2 shows an example of the results obtained from Case IIIa, where the data for each pellet type are plotted on a χ - AR^{-1} map as reported by Lau et al. (2014). Similar distributions were obtained for other Cases. With the exception of spheroids (Fig. 2(h)), the data sets overlap and occupy a broad band below the locus for an ideal half-cigar (Table 2). The majority of spheroids feature AR^{-1} values >0.8 , corresponding to the general observation reported above that round pellets are associated

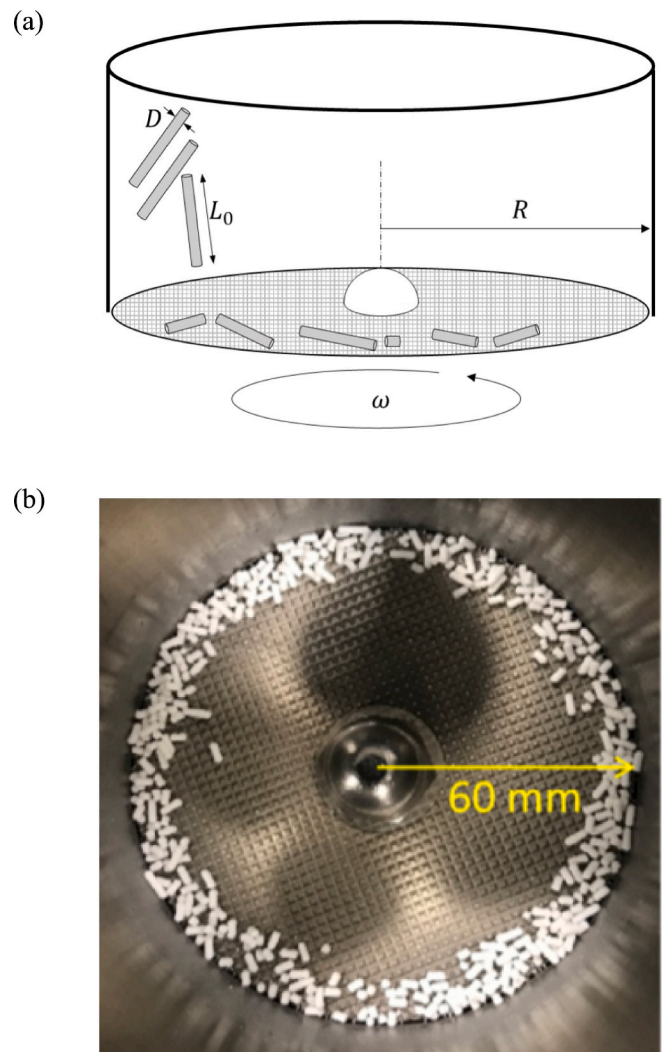










Fig. 1. (a) Schematic and (b) photograph, plan view, illustrating spheroniser operation. Identical cylindrical extrudates of length L_0 and diameter D are added to the spheroniser plate of radius R which spins at angular velocity ω .

with $AR \leq 1.2$. Curiously, the shapes featuring bulbous ends, namely flasks, dumb-bells and bulbs (Figs. 1(d), (e) and (f), respectively) lie mostly between the loci for an ideal half-cigar and a rod. Circularity does not, therefore, support reliable differentiation between the categories, as reported by Bryan et al. (2015). Other quantitative measures were also considered, including machine learning approaches, but these were no more effective than visual inspection, as determined by peer review by up to 6 individuals. These comparisons were performed by using the categorisation data from one individual as the standard (for a number of cases). The data set was split into a training fraction (up to 80%) and a test fraction, and categorisation performed either by the other individuals or by the automated methods. The agreement was summarised in success matrices (data not reported). Manual categorisation had a higher successful categorisation rate, especially for shapes which were less prevalent in the population, and was used to categorise the end shape combinations in Table 2.

Table 3 summarises the occurrence of the different shapes for each pellet length and Case. The data sets exhibit a matrix form, with zero and non-zero entries, and follow a similar sparsity pattern, viz. zero entries in the left-hand lower quadrant, below a common diagonal, and the largest entries appearing in the right-hand upper quadrant. Features common to all Cases include:

Table 2

Pellet shape classification. End labels: s – square; r – rounded (radius similar to initial pellet); b – bulbous (rounded, radius greater than initial pellet). The χ -AR⁻¹ relationships for rods, cigars and half-cigars are plotted in Fig. 2. Relationships marked † are not reported as these were found to offer little insight.

Shape	Label	Image	End pair	χ -AR relationship
Rod	R		s-s	$\chi_R = \left(\frac{\pi}{AR}\right) \frac{1}{\left(1 + \left(\frac{1}{AR}\right)\right)^2}$
Cigar	C		r-r (AR > 2)	$\chi_C = \left(\frac{\pi}{AR}\right) \frac{\left[1 + \left(\frac{1}{AR}\right) \left(\frac{\pi}{4} - 1\right)\right]}{\left[1 + \left(\frac{1}{AR}\right) \left(\frac{\pi}{2} - 1\right)\right]^2}$
Half-cigar	H		r-s	$\chi_H = \left(\frac{\pi}{AR}\right) \frac{\left[1 + \left(\frac{1}{AR}\right) \left(\frac{\pi}{8} - \frac{1}{2}\right)\right]}{\left[1 + \frac{\pi}{4} \left(\frac{1}{AR}\right)\right]}$
Flask	F		b-s	†
Bulb	U		b-r	†
Dumbbell	D		b-b	†
Bispheroid	B		b-b	†
Spheroid	S		r-r (AR ~ 1)	~1

- (i) Shapes R, H and C, occur for all pellet lengths (apart from three zero entries in Case IV, one in Case I and one in Case IIIb).
- (ii) Shapes F, U, D, B and S do not occur for pellet lengths >3.
- (iii) For shapes R and H, the highest proportion occurs for pellet lengths of 1 and 2.
- (iv) For shapes C, U and D, the highest proportion occurs for a pellet length of 2.
- (v) For shapes B and S, the highest proportion occurs for a pellet length of 1.

There is some evidence that for the increased loading (Case IIIb) and highest rotational speed (Case IV) there are more zero data entries in the left-hand lower quadrant, with a subsequent ‘shifting’ of the non-zero values to the right-hand upper quadrant. It appears that rotational speed and loading may have some influence on the size and shape distribution of the final product, as per the analysed classifications, although further experimentation would be required to confirm this. Further investigations, generating thousands of pellet images per test, would be facilitated by the development of automated shape classification, which is the subject of current work. The above observations were used to set some of the kinetic parameters in the 2-D PBM to zero.

Fig. 3 summarises the change in pellet length and shape over time. Fig. 3(a) shows the trend reported in [12], namely the rapid initial disappearance of long rods; the generation of appreciable number of pellets of length 3 and 2; followed by the fast depletion of the former and the slow decay in the latter. For this Case, only pellets of length 1 and 2 were present at the end of the test ($\tau = 3.5 \times 10^7 \text{ s}^{-2}$). The corresponding shape data are presented in Fig. 3(b). The initial batch of rods is converted to smaller numbers of rods as a result of breakage and these tend to become half-cigars or cigars, forming a pool of about 60 pellets, from which more complex shapes appear. With the exception of the rods (see above) and spheroids, which exhibit a steadily increasing trend, each category exhibits birth followed by decay. The loci on the plots show the trends predicted by the 2D PBM population balance model and serve as guides to the eye. Similar trends were observed for the other Cases [see Supplementary Information S2].

Fig. 4 presents the classification data together for Cases IIIa ($N_0 = 20$) and IIIb ($N_0 = 80$). Similar trends are evident: the larger number of pellets in the latter case results in less granular distributions. Relatively few pellets of length 5 and 4 are formed, as noted in Table 3, indicating that they, like the length 6 rods, tend to break rapidly. The population of length 3 pellets persists for longer, indicating that the breakage rate is related to length, as discussed in [12]. For this Case, at scaled times

beyond $\tau \sim 10^7 \text{ s}^{-2}$ the pellets are mostly of length 1 and 2, and while there is some breakage (associated with a change in the number of pellets) after this time, most of the transitions are associated with rounding-induced changes in shape. The corresponding plots for I, II and IV are provided in Supplementary Information S3.

2. Population Balance

The two-dimensional population balance scheme is presented in Fig. 5(a). It is based on a branching-paths model which captures the evolution of each end independently, without inferring a principal or preferred path for shape evolution. Discretising pellet length into 6 equal width bins, as used by Wang et al. [12], yields the system of 48 coupled ODEs in Appendix 1. The following assumptions were made:

- (i) Shape evolution does not affect the pellet length, e.g. rounding of a cigar of length i does not generate a dumbbell of length $i-1$.
- (ii) Each end evolves independently.
- (iii) Bispheroids and spheroids do not break. Inspection of the pellets did not reveal any shapes which would have been caused by breakage of a bispheroid or a spheroid.
- (iv) Breakage yields two daughter pellets, each with a square end and the other corresponding to one of the ends of the parent pellet. Breakage induced by bending is expected to give two fragments with straight fracture planes, the length of which is determined by the maximum bending stress. No experimental observations supported an alternative breakage mode, e.g. one yielding three fragments.
- (v) The kinetic constant for a breakage event does not depend on the outcome, i.e. the distribution of ends between the daughter pellets. For example, a half-cigar of length 5 could break to give a half-cigar of length 1 and a rod of length 4, or a rod of length 1 and half-cigar of length 4 (Fig. 5(b)). The probability is assumed to be the same, and the rate is written as $-2k_{5H,4H,1R}n_{5H}$ in the dn_{5H}/dt balance, i.e. $k_{5H,4H,1R} = k_{5H,4R,1H}$.

Assumption (i) represents a simplification, and is valid when breakage is rapid. Otherwise, conservation of volume requires that the transition from a rod or cigar to a dumbbell, for example, must be accompanied by a reduction in length, and this will result in the pellet being allocated to the next size category. The trajectories in $\chi - AR^{-1}$ space (Fig. 2) associated with several of these transitions were calculated but the results offered little insight and are not reported.

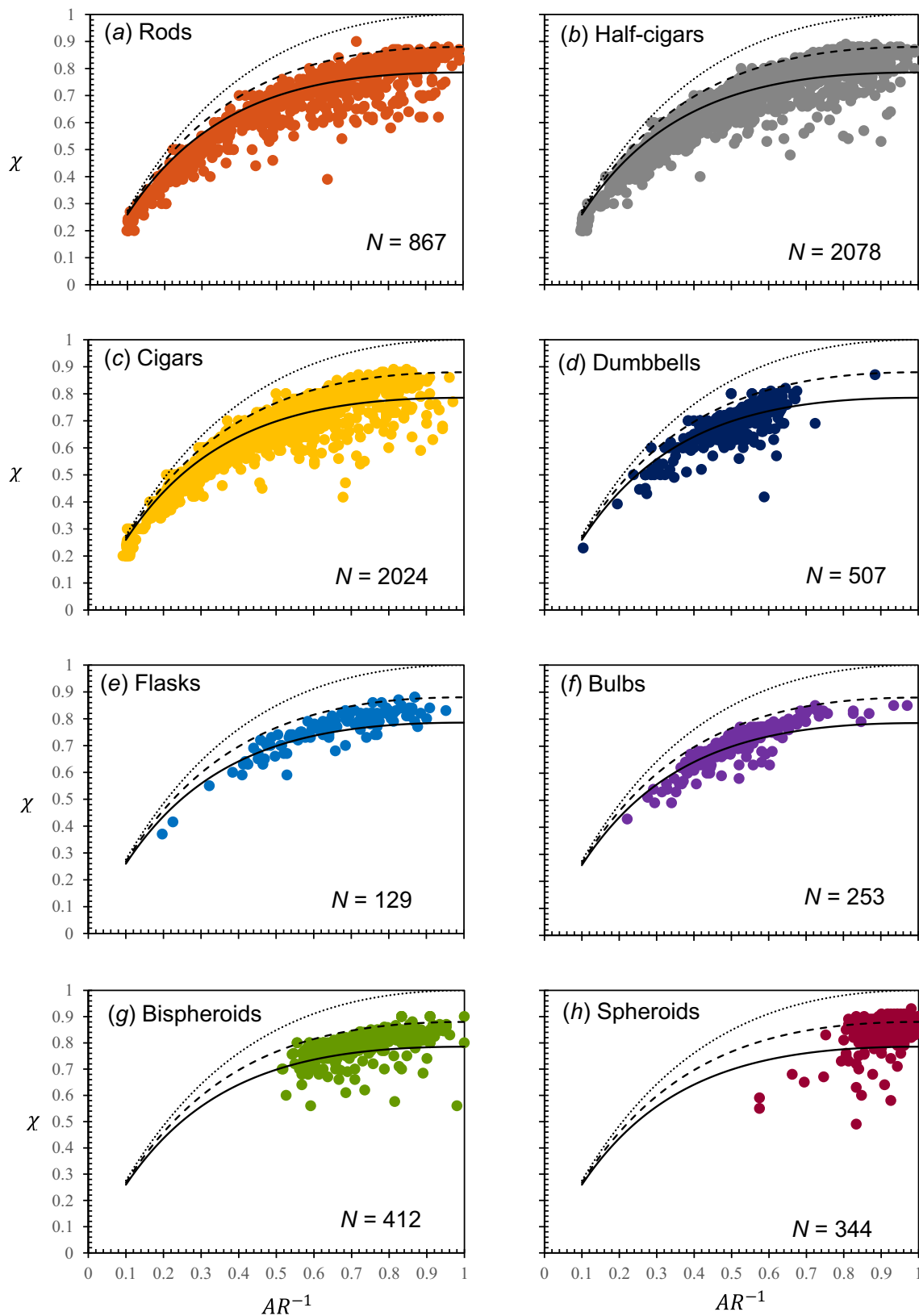


Fig. 2. Example of classification of pellets for Case IIIa, sorted into the categories in Table 2 by visual inspection. AR is equivalent to pellet length. Loci show the analytical $\chi - AR^{-1}$ relationships in Table 2 for: rod – solid line; half-cigar – dashed; cigar – dotted.

Table 3

Frequency of shapes for each pellet size, reported as percentage of each category as a fraction of the total number of pellet images studied over all time intervals, N_{all} .

	Pellet size Shape, label	6	5	4	3	2	1
Case I $N_{all} = 2541$	R - Rod	3.9	0	0.3	0.3	3.9	14.7
	H - Half-cigar	1.6	0.1	0.5	1.4	12.2	15.2
	C - Cigar	3	0.1	0.3	0.8	19.3	2.9
	F - Flask	0	0	0	0	0.3	2.1
	U - Bulb	0	0	0	0	3.4	1.3
	D - Dumbbell	0	0	0	0	3.3	1.1
	B - Bispheroid	0	0	0	0	0	2
	S - Spheroid	0	0	0	0	0	5.9
Case II $N_{all} = 2502$	R	3	0.1	0.3	1	6.3	12.4
	H	1	0.1	0.6	2	19.7	18.2
	C	1.1	0.1	0.4	2.2	16.8	2.8
	F	0	0	0	0	0.4	1.8
	U	0	0	0	0	2.2	0.6
	D	0	0	0	0	1.1	0.4
	B	0	0	0	0	0	1.2
	S	0	0	0	0	0	4.2
Case IIIa $N_{all} = 6145$	R	2	0.1	0.6	1.7	4.3	5.7
	H	0.9	0.2	0.9	3.6	12.9	13.1
	C	1	0.2	0.7	3.3	17.7	7.4
	F	0	0	0	0	0.6	1.2
	U	0	0	0	0.1	3	0.7
	D	0	0	0	0.2	6.2	0.7
	B	0	0	0	0	0.7	5.1
	S	0	0	0	0	0	5
Case IIIb $N_{all} = 4060$	R	3.9	0	0.7	2.6	18.3	9.8
	H	0.3	0.2	1.6	6	25.3	4.6
	C	0.4	0.2	1.2	5.2	13.2	0.6
	F	0	0	0	0	0.8	0.4
	U	0	0	0	0	1.1	0.1
	D	0	0	0	0	0.1	0
	B	0	0	0	0	0.1	0.3
	S	0	0	0	0	0	2.9
Case IV $N_{all} = 2418$	R	2.6	0.1	0.4	2.4	16.5	14.2
	H	0	0.1	0.2	1.9	18.8	10.5
	C	0	0	0.2	0.8	16	5.9
	F	0	0	0	0	1.2	0.4
	U	0	0	0	0	2	0.3
	D	0	0	0	0	0.9	0.3
	B	0	0	0	0	0	0.5
	S	0	0	0	0	0.2	3.6

Fig. 5(b) shows the combination of outcomes for a half-cigar of length 5, with number n_{5H} at time τ . The ODE describing the evolution of n_{5H} is

$$\frac{dn_{5H}}{d\tau} = -n_{5H} \left(\underbrace{2k_{5H,4H,1R} + 2k_{5H,3H,2R} + k_{5H,5C} + k_{5H,5F}}_{\text{breakage}} \right) + \underbrace{n_{5R}k_{5R,5H} + n_{6C}k_{6C,5H,1H} + n_{6H}k_{6H,5H,1R} + n_{6B}k_{6B,5H,1H}}_{\text{formation}} \quad (2)$$

Prior to simplification, the model had over 130 unknown kinetic constants. Employing a finer discretisation scheme (e.g. 10 bins, each of interval width D) would increase this number further, and also result in a sparse distribution where more bins had few pellets assigned to them.

3. Numerical methods

The ODEs were solved numerically via the 4th order Runge-Kutta method using Matlab2022a with a scaled time-step size of 0.05×10^7 s⁻² in most cases. The Matlab code is provided as Supplementary Material S4. Identifying the values of the kinetic constants is an

optimisation problem. The objective function was the sum of the square of the differences between the predicted and measured number of pellets in each category (or set of categories) across all the time intervals measured. A three-step approach was used:

- (i) The one-dimensional PBM of Wang et al. (Supplementary S1), with 9 kinetic constants, was solved to identify the sum of the breakage constants for each size fraction. Different optimisation methods were used in this work to that used previously, so the values were expected to differ to some extent. The range of allowable values was constrained at $0-20 \times 10^{-7}$ s⁻², based on the largest value of kinetic constant reported in [12]. Genetic algorithms (GA) and boundary constraint algorithms (BCA) were both considered, with the latter proving more robust (better goodness of fit, result almost independent of starting set). The settings for each algorithm are reported in Table 4. The improvement in goodness of fit, R^2 , for the five Cases is reported in Table 5. This

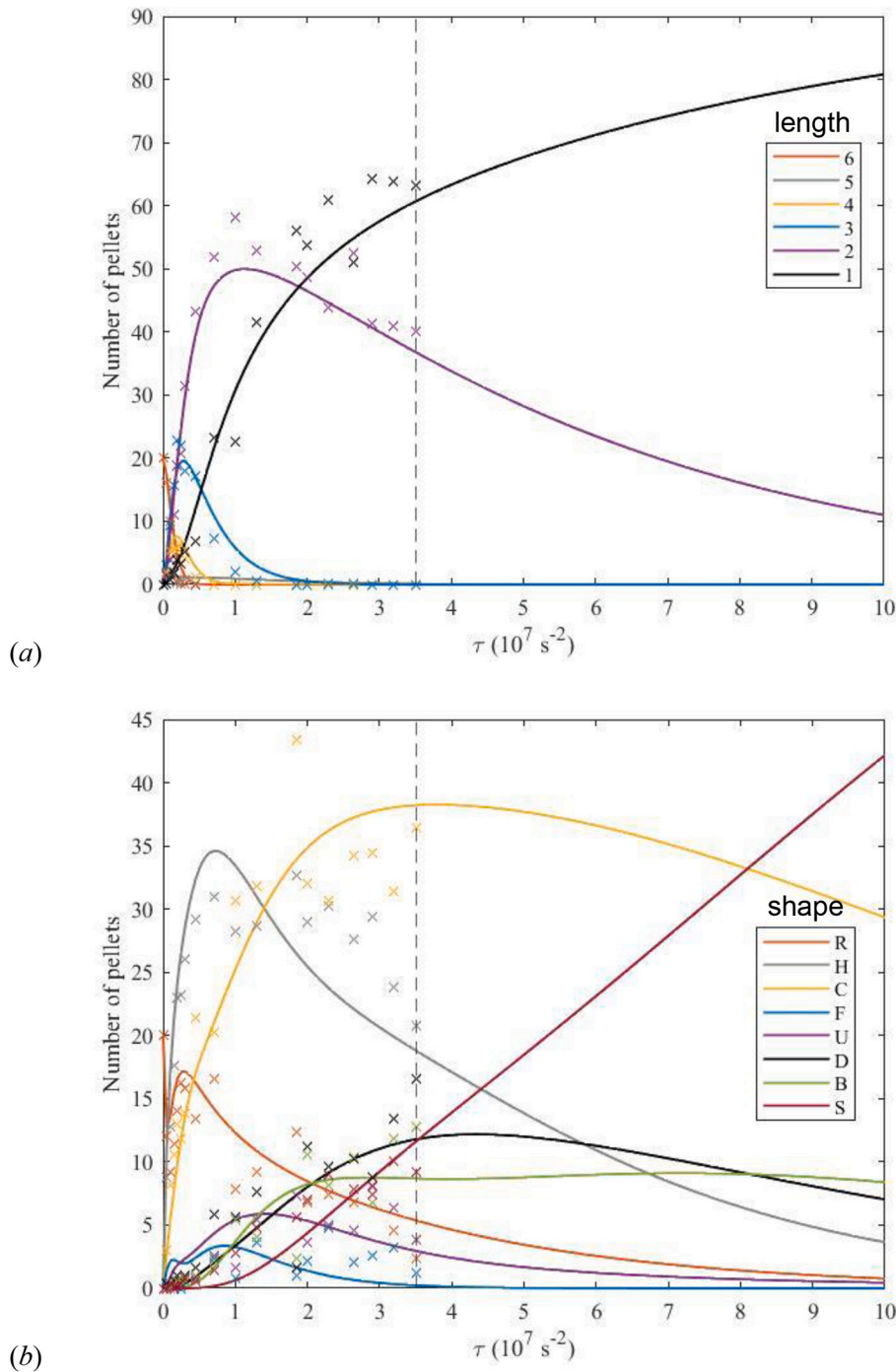


Fig. 3. Evolution of pellet (a) length and (b) shape for Case IIIa. Loci show the trajectories for the 2D PBM with parameters obtained by fitting to the data set. Vertical dashed line indicates limit of experimental data: beyond this the loci show the model extrapolation. The colours in (b) correspond to those in Fig. 2.

step provided values of the combined breakage kinetic constant for pellets of length i , b_i , Eq. (3), that were used as constraints in step (ii). For example, the change in the number of pellets of length 6 is written as

$$\frac{dn_6}{d\tau} = -(k_{6,5} + k_{6,4} + k_{6,3})n_6 = -b_6n_6 \quad (3)$$

(ii) In the 2-D PBM, a two-step approach was used to identify the kinetic parameters. In the first step, the breakage constants were identified by matching the instantaneous net rates of breakage

with those given by the 1-D model. In time interval q the 1-D net breakage rate of pellets of length i , $B_{i,1D}$, is given by

$$B_{i,1D}(q) = b_i n_i(q) - \sum_{m>i} k_{m,i} n_m(q) \quad (4)$$

where the number of pellets in length class i , n_i , is given by summing across all shapes of length i :

$$n_i(q) = \sum_{s=R,H,\dots,S} n_{i,s}(q) \quad (5)$$

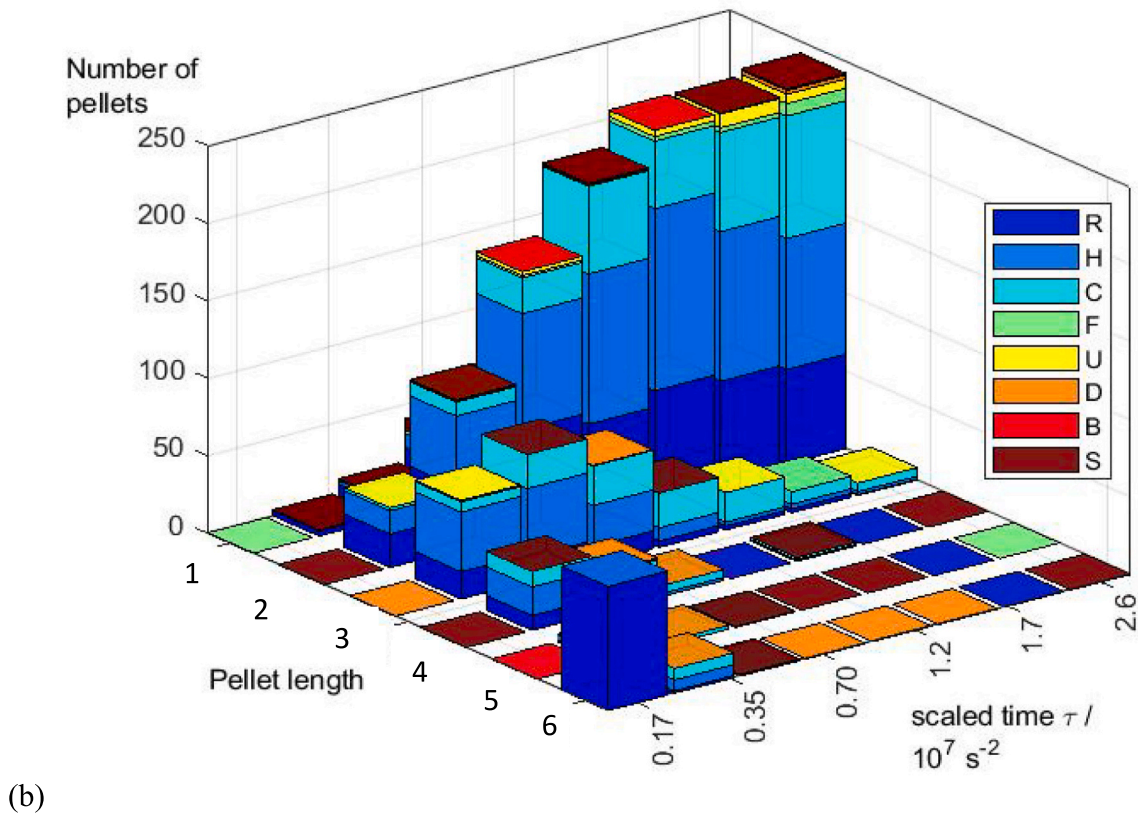
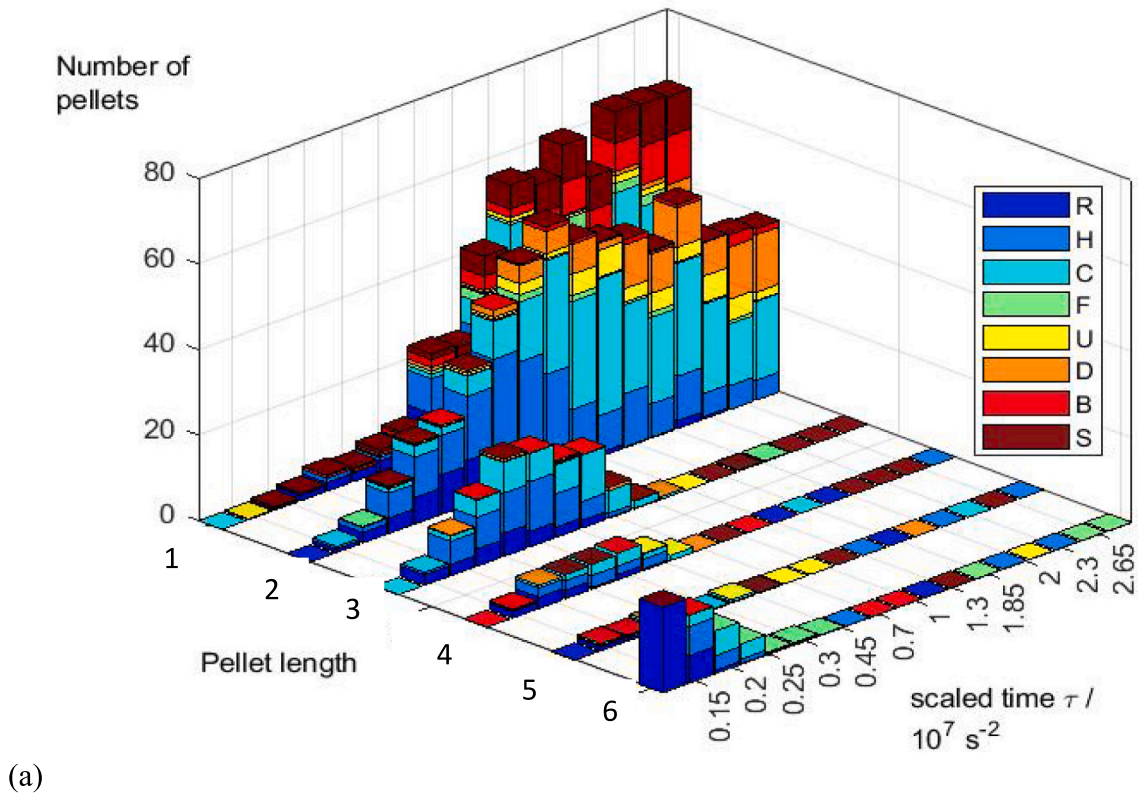


Fig. 4. Evolution of pellet length and shape for (a) Case IIIa and (b) Case III. Note non-linear scaled time axis. Colour indicates category. Loci in show.

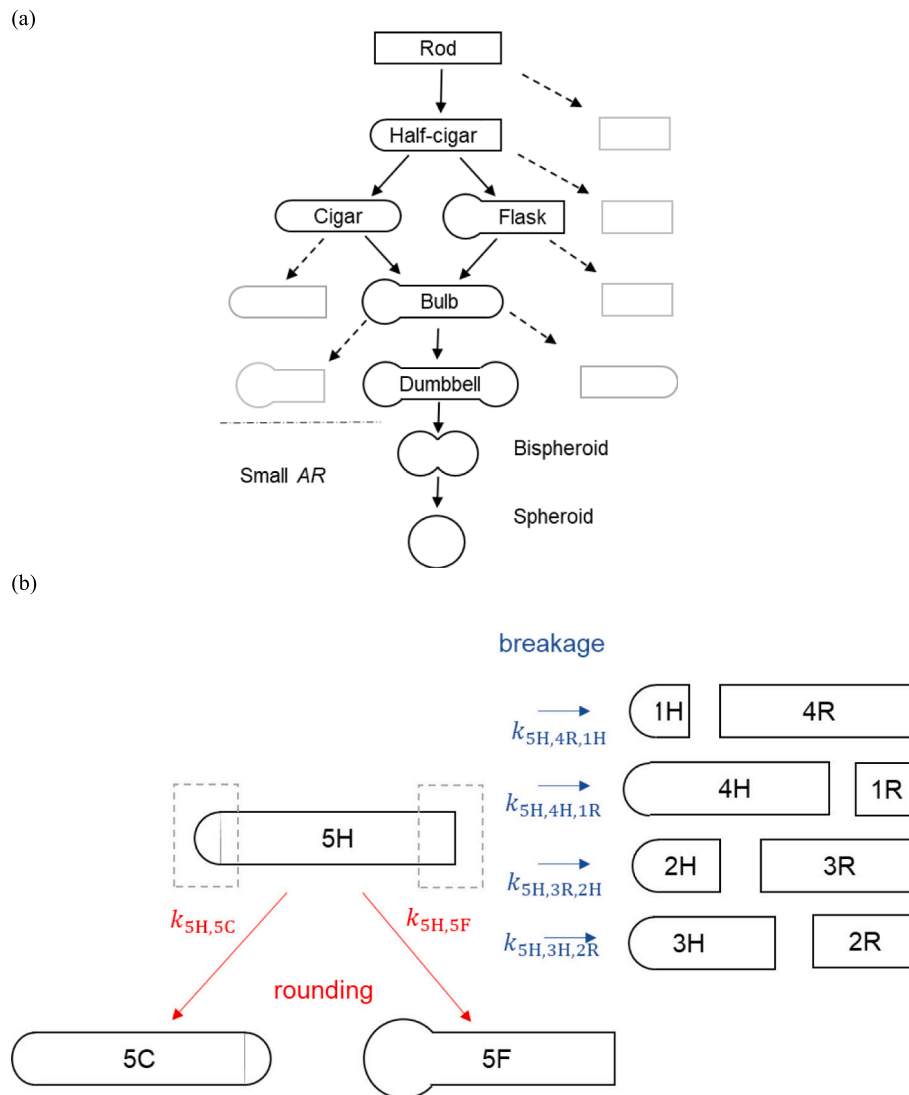


Fig. 5. Two-dimensional population balance model. (a) Schematic of shape and size evolution. Solid arrows indicate shape transitions (rounding); dashed arrows indicate size transition (breakage). (b) Example: pellets formed from a half-cigar of length 5.

Table 4
Optimisation algorithm settings.

Algorithm	Parameter	Value
Genetic algorithm (GA)	Population	10,000
	Number of generations	25
	Tournament size	256
	Mutation rate	1%
	Number of elites	1
Boundary constraint (BCA)	Population	1000
	Iterations	100
	Generations	breakage 25
		breakage & rounding 100
Particle swarm (PSO)	Number of candidate solutions	10,000
	Cognitive learning factor	0.1
	Social learning factor	0.1
	'Momentum of particle' or 'inertia weight'	0.8
	Generations	breakage 25
		breakage & rounding 100

Table 5

Comparison of goodness-of-fit for Case IIIa the 1D PBM (length alone, not shape) with the constants (i) reported by Wang et al. [12] and (ii) obtained with the BCA.

Pellet length	Number of pellets in fit	R^2		Change
		Wang et al.	BCA	
–	–			
1	2498	0.908	0.961	0.053
2	2961	0.884	0.946	0.062
3	591	0.806	0.911	0.105
4	151	0.800	0.897	0.097
5	33	–13.09	–0.376	12.72
6	181	0.757	0.940	0.183
all	6415	0.941	0.976	0.035

The 2-D breakage of pellets in a given length class at time interval q is given by

$$B_{i,2D}(q) = \sum_{l=i-1, i-2, \dots, 1}^{\lceil i/2 \rceil} \sum_{s_1, s_2, s_3 \in R, H, \dots, S} k_{is_1, ls_2, (i-l)s_3} n_{i, s_1}(q) - \sum_{m=6, 5, \dots}^{m>i} \sum_{s_1, s_2, s_3 \in R, H, \dots, S} k_{ms_1, is_2, (m-i)s_3} n_{m, s_1}(q) \quad (6)$$

where the RHS includes all the permitted shape combinations. The experimental values of n_{i, s_1} and n_{m, s_1} were used to evaluate $B_{i,1D}$ and $B_{i,2D}$ for each interval. The 2-D kinetic constants were then determined by an optimisation (using the Microsoft Excel® inbuilt Solver function) to identify the most likely set of values, with objective function

$$Obj = \sum_{q=1, \text{end}} \sum_{i=1}^6 \frac{(B_{i,2D} - B_{i,1D})^2}{(B_{i,2D} - \bar{B}_{i,1D})^2} \quad (7)$$

where $\bar{B}_{i,1D}$ is an average of the 1-D breakage rates for size fraction i , and the denominator serves to scale the contributions from each fraction.

- (iii) In the second step, the remaining 57 kinetic constants for rounding were identified by fitting the 2D PBM to the data sets, the breakage constants having been determined in (ii). A particle swarm optimisation (PSO, settings in Table 4) approach was found to give robust performance.
- (iv) Steps (ii) and (iii) yielded a solution which is likely to be near a local optimum. The solution was improved by fitting the full PBM, with all 96 kinetic constants as variables, to the data using a gradient descent (GD) algorithm. The values identified in (ii) and (iii) were used as the starting set. The GD approach is more efficient in identifying a local optimum, while the PSO serves to find a better estimate of a global optimum across the full parameter space. The improvement in R^2 given by the GD step was approximately 6.5%.

4. Results and discussion

4.1. Shape and size trends – 1D PBM

Plots such as Fig. 3 show that the long pellets (of length 5 and 6) undergo rapid breakage and therefore have little time to undergo rounding, while Fig. 4 details how pellets of length 2–4 undergo more appreciable rounding as the rate of breakage decreases with pellet length. Fig. 3 also shows that the $\omega^3 t$ scaling collapses the data to a similar timescale. The loci in Fig. 3 are similar to those reported in [12], and Fig. 6 compares their breakage constants with those obtained for the

1-D PBM obtained by the BCA. Table 5 compares the goodness of fit for the two approaches and reports the number of pellets in each length category. The BCA improved the fit for all pellet sizes. The improvement of fit for pellets of length 5 is still associated with a negative value of R^2 , indicating that the reliability of the description is poor. Table 5 shows that there were relatively few pellets of length 5 (33, compared to 151 of the next most frequent, of length 4). The two approaches yield noticeably different results for length 5 pellets, with the BCA setting $k_{6,5,1}$ to zero, in effect predicting that length 6 pellets will not break to form ones of length 5. Furthermore, the large BCA value for $k_{5,3,2}$ indicates that any length 5 pellets formed would break rapidly. In short, the BCA has accepted the penalty associated with poor prediction of n_5 in order to optimise the global performance. This could be overcome by attaching a weighting to some of the n_5 values. This represents one of the areas in which the optimisation calculation could be improved. In steps (ii) and (iii) breakage to form length 5 pellets was allowed.

It is also noticeable that both modelling approaches set $k_{5,4,1}$ to zero, suggesting that longer pellets will break nearer their midpoint rather than at an end. Fig. 6 shows similar values for the breakage constants for the shorter pellets ($k_{4,2,2}$, $k_{3,2,2}$ and $k_{2,1,1}$).

Owing to the nature of the fitting function and the large number of ODEs and constants involved, there is a strong likelihood of the parameter set identified constituting an ‘over-fit’ [14]. Minimising the number of constraints imposed on the model was considered to be preferable, to reduce bias in the fitting. The interpretation of the results consequently focuses on the general trends. Given the intrinsically random nature of breakage, an extensive experimental programme would be required in order to generate the large body of data required to reduce over-fitting.

4.2. 2-D PBM: breakage

The parameterisation procedure yielded 5 sets of kinetic constants, the values of which are provided as Supplementary Material S5. Fig. 7(a) shows that the sum of breakage constants (e.g. Eq. (5)) increased with pellet size, as reported by Wang et al. for their 1D PBM. A Friedman test performed on the ranked order of the likelihood of breakage for each pellet for the five Cases at the 5% significance level indicated that the plate rotational speed had no effect on the ranking for each pellet length. This indicates that there was no bias with rotational speed and again indicates that the $\omega^3 t$ scaling has captured the influence of this process parameter. The confidence in this result is not high owing to only five Cases being considered. Cases IIIa and IIIb featured a four-fold difference in the initial number of pellets. The sum of breakage constants in Fig. 7(a) lies within the scatter obtained with the other Cases, which is consistent with the breakage mechanism being determined by pellet-pelletiser (wall or plate) collisions with little contribution from pellet-pellet collisions.

Fig. 7(b) presents the distribution of breakage constants for each pellet length. The likelihood of breakage of a length 2 pellet is consistently smaller than the other values for each Case, indicating that most pellets form a pellet of length 2, which then are then slowly converted to length 1. These results indicate that the transition between breakage and rounding is associated with the formation of pellets of length 2. This is consistent with Wang et al.’s findings.

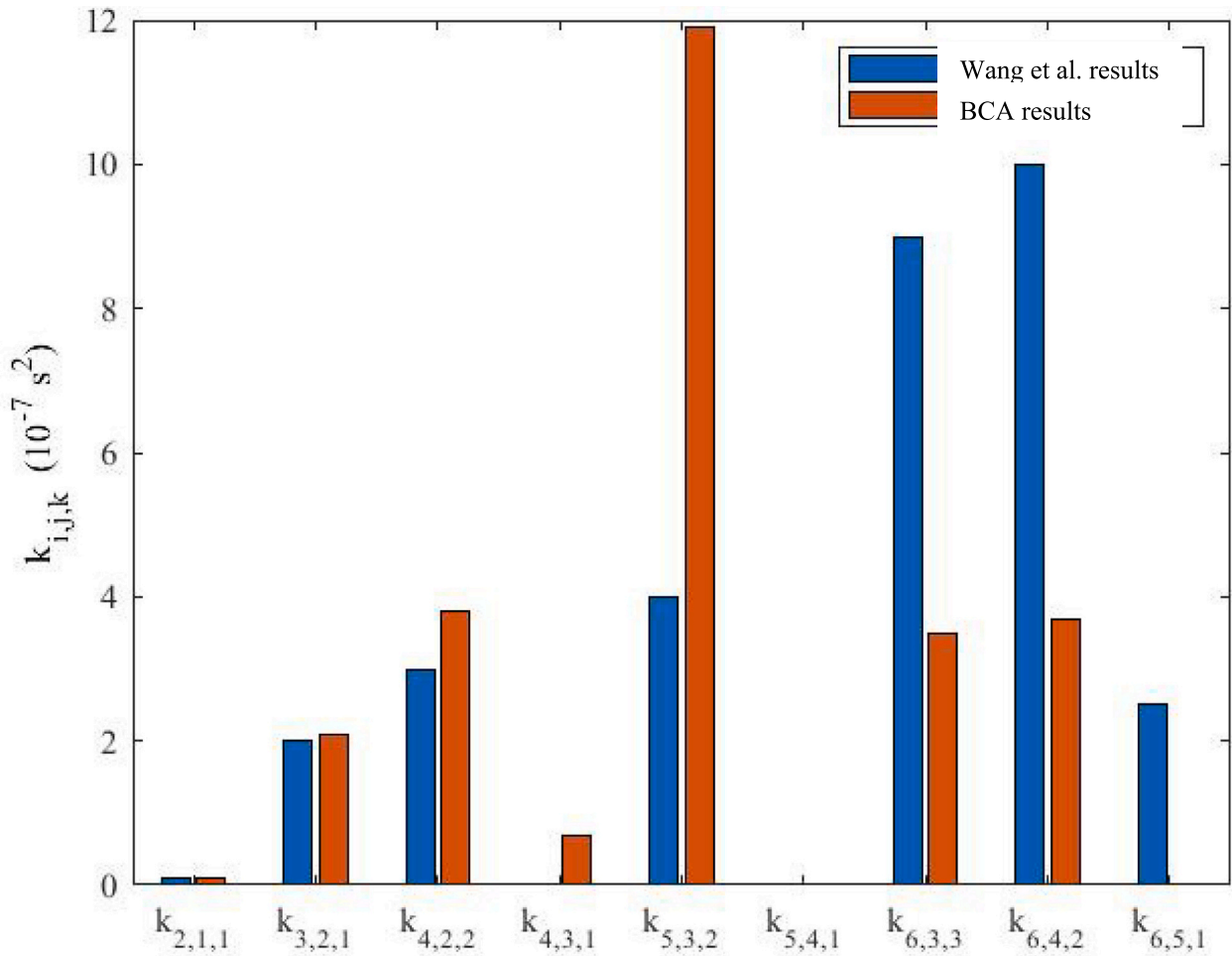


Fig. 6. Comparison of 1D PBM model breakage kinetic constants with those reported by Wang et al. [12].

4.3. Rounding

The sum of rounding kinetic constants is reported in Fig. 8(a). There is noticeable scatter between Cases, as with the breakage constants in Fig. 7. The values lie in a similar range, again suggesting that the $\omega^3 t$ scaling captures the influence of rotational speed. There is no strong contribution from pellet length on rounding with the exception of pellets of length 1, associated with the generation of bispheroids and spheroids. Statistical analysis, namely p-tests at the 5% significance level, indicated that the overall likelihood of rounding for a particular Case did not deviate significantly from the mean of all the Cases.

The type of rounding transition is compared in Fig. 8(b). The values of $k_{R,H}$ and $k_{H,C}$ are similar, which is expected as the transition involves the rounding of a square end to a spherical one. The values of $k_{H,F}$ and $k_{C,U}$, are likewise similar, involving the generation of a bulbous end. The values of $k_{F,U}$ and $k_{U,D}$ do not follow the trends in these pairs. This may be due to the fitting procedure not capturing the later stages of rounding reliably, or it being relatively insensitive to these steps as the number of pellets associated with the transitions is low: <2% of the total number of pellets were classified as flasks, while 4% were ‘bulbs’. The figure suggests that the likelihood of a square end forming a round end is higher than a rounded end forming a bulbous one, as follows: less plastic deformation work is expected for the former transition, so fewer collisions would be required to provide the kinetic energy: if the rate of collisions is independent of shape, this would translate into a larger rate constant.

The likelihoods of the final stages of rounding – the flask to bulb, bulb to dumb-bell and dumb-bell to bispheroid transitions – are all

larger than those for the initial stages. With the exception of Case IIIb ($N_0 = 80$) the dumb-bell to bispheroid constant is larger than the corresponding bispheroid to spheroid constant, which is consistent with the final rounding stage being rate limiting, as suggested by Eq. (1).

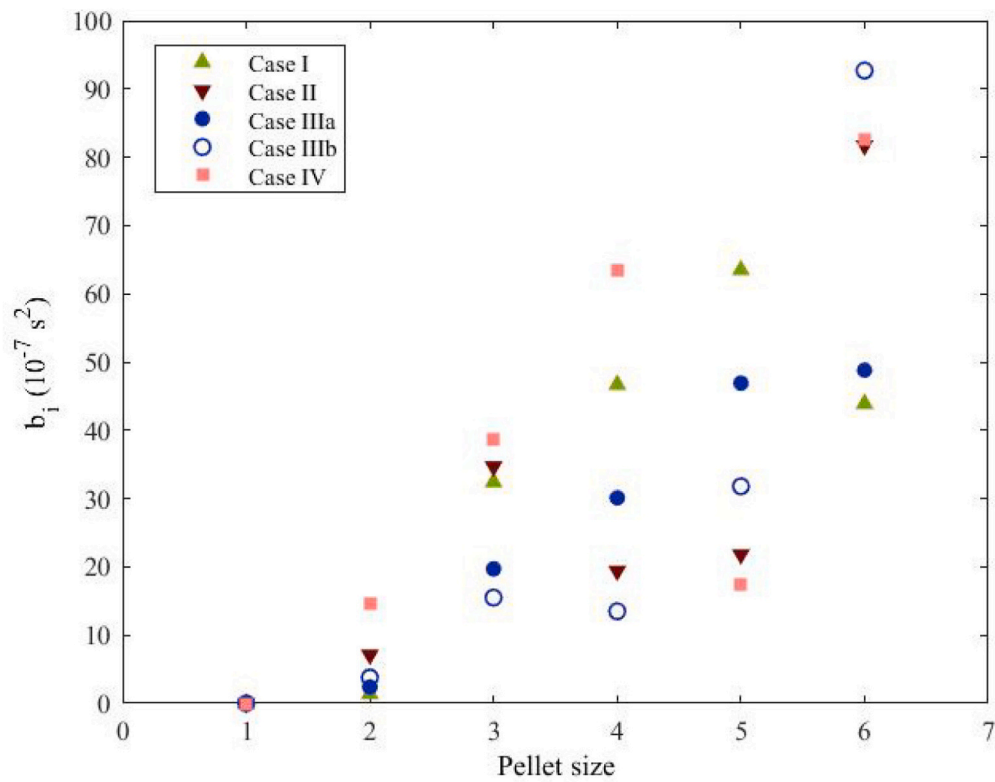
Fig. 9 summarises the inferred behaviour patterns, comparing the estimated likelihoods of breakage and rounding for each Case. The net likelihood of breakage per collision is given by

$$p_{B,i} = \frac{b_i - r_i}{b_i + r_i} \quad (8)$$

where b_i is the sum of breakage kinetic constants for pellets of length i and r_i is the corresponding likelihood of rounding. For tests with $N_0 = 20$ (Cases I-IIIa, IV) breakage dominates for pellets of length 3 and greater. For Case IV, with $N_0 = 80$, the changeover is not so clear and rounding dominates for pellets of length 1 ($AR < 1.66$). Both outcomes are consistent with Evers et al.’s observation of AR_0 values in the range 1.4–2.4 [11]. They reported AR_0 values after 30 s, for loadings of 16–100 kg m⁻³. At lower speeds, AR_0 did not vary much consistently with loading. Their AR_0 values for $d_p = 0.12$ and 0.25 m after 30 s (corresponding to $\tau > 20 \times 10^7$ s⁻², i.e. well into the rounding stage) decreased with loading and thus the expected number of pellet-pellet collisions.

At higher loadings, there are more pellets in the toroidal bed (see N_{tm} in Table 1) and pellet-pellet collisions are expected to become more important. The assumption of a first order kinetic scheme would require revisiting for detailed modelling of tests with higher loadings as the first order treatment assumes that the frequency of collisions is independent of the number of other pellets. Introducing collisions with other pellets

(a)



(b)

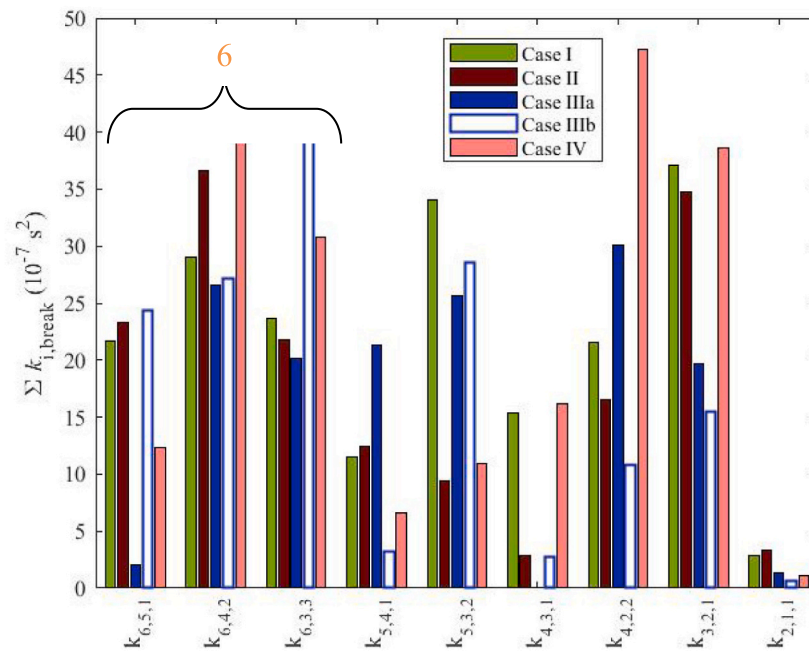
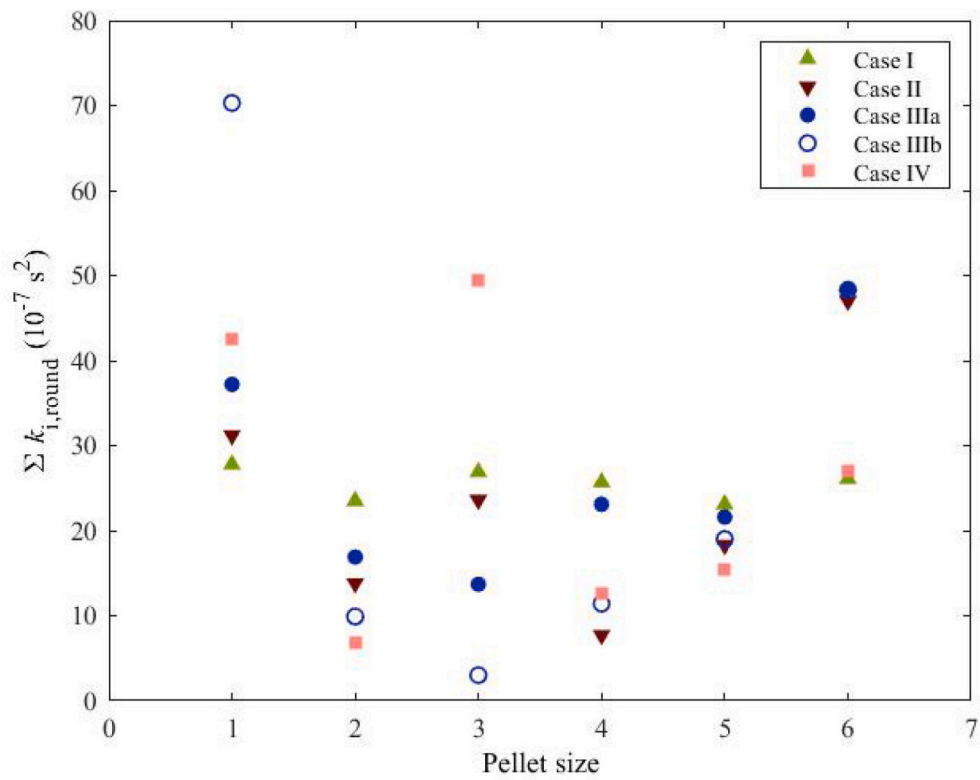


Fig. 7. Breakage constants obtained for the 2D PBM. (a) Effect of pellet length on the sum of all breakage constants for pellets of that length; (b) Sum of breakage constants for each pellet breakage combination, ordered in sequence of events.

(a)



(b)

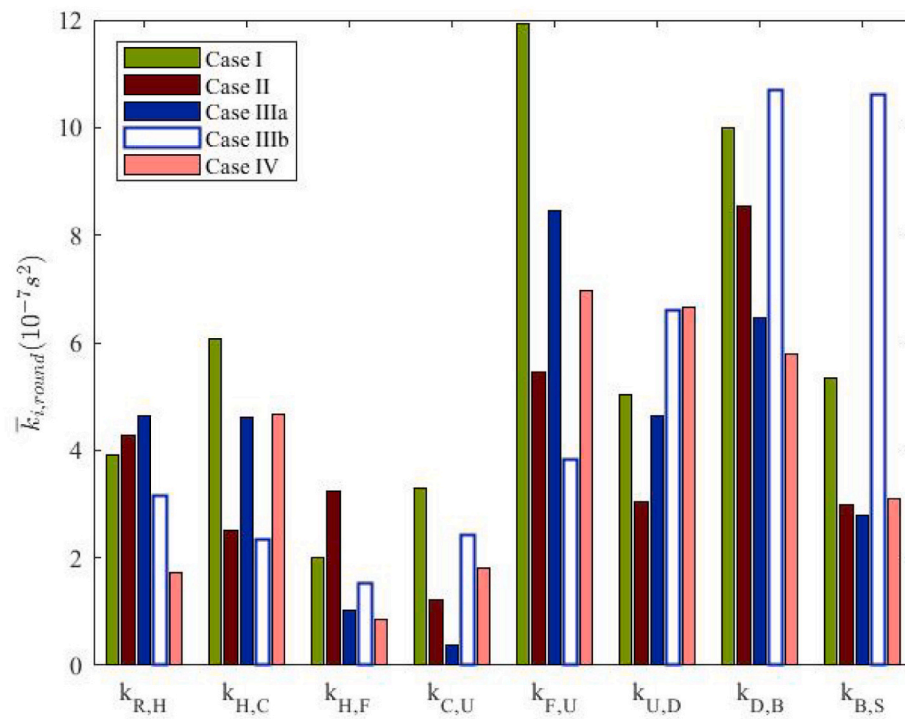


Fig. 8. Rounding constants obtained for the 2D PBM. (a) Effect of pellet length on the sum of all rounding constants for pellets of that length: (b) Sum of rounding constants for each combination, ordered in sequence of events.

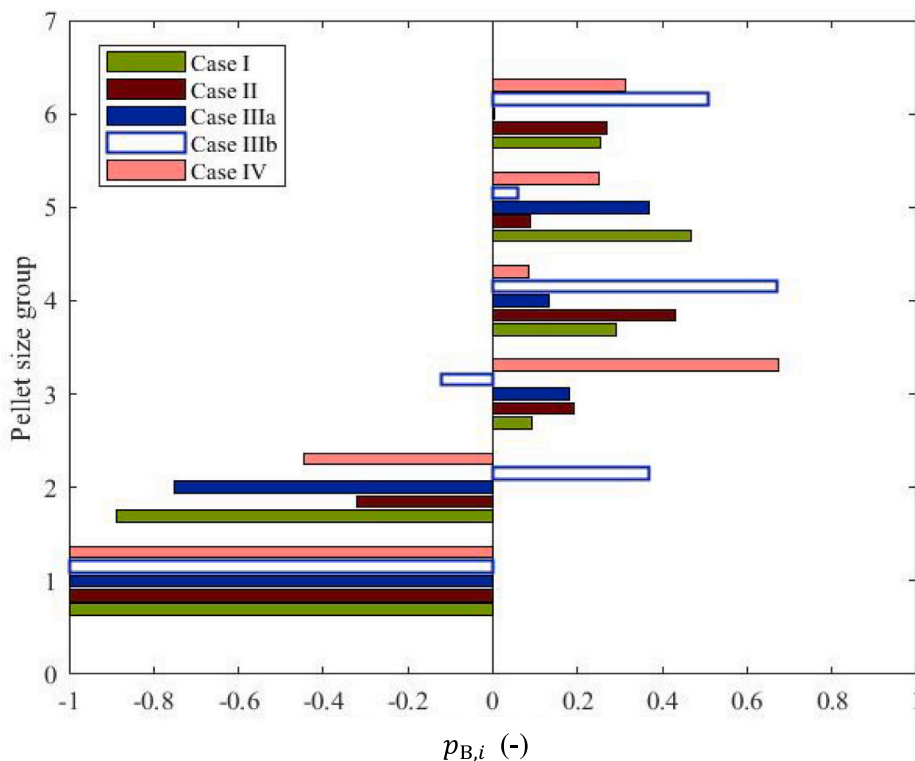


Fig. 9. Effect of pellet size on net likelihood of breakage, Eq. (4).

as opposed to collisions with the wall or friction plate suggest a second order process. This represents a topic for future work.

4.4. Discussion

This study represents an initial attempt to capture the simultaneous evolution of pellet size and shape during the initial stages of spheronisation. There are several facets in which the calculations could be improved, such as the use of more robust optimisation algorithms, better suited for sparse data sets, for instance by including weightings as mentioned above. The model generates a large number of kinetic constants and in this study is fitted to a relatively small number of data points which are subject to noticeable scatter. The latter is expected because breakage is inherently a stochastic process. This could be addressed by collecting more, larger data sets but this requires a reliable shape characterisation tool to be available as otherwise the uncertainty in the shape labelling dominates.

Rounding is presented as a continuous process and this assumption may not be correct. Rounding and breakage are assumed to be independent and this is also likely to be inaccurate: as repeated collisions generate a dumbbell it is likely to become shorter.

The experiments feature small numbers of extrudates and consequently modest numbers of pellets. The results demonstrate that breakage and rounding occur simultaneously, but the small number of extrudates meant that collisions were dominated by collisions with walls and the spheroniser plate rather than the pellet-pellet collisions that will dominate the dynamics of a commercial spheronisation operation. Fig. 8 shows that case IIIb (with $N_0 = 80$) exhibits more rounding for pellets formed later in the process, which would arguably be expected from pellet-pellet collisions. Imposing a first order kinetic scheme on the process at this stage, when a second order scheme would be more appropriate, should be revisited and tested using more data sets. As highlighted above, such investigations will require reliable and efficient pellet shape characterisation tools.

5. Conclusions

A two-dimensional population balance model has been developed, which quantifies the evolution of pellet size and shape during the initial stages of spheronisation of microcrystalline cellulose/water extrudates. Methods to fit the model to experimental data were developed, which enabled the extraction of process parameters describing the independent mechanisms of breakage and rounding of the pellets.

The inherently first-order model was based upon an extension of previously reported kinetic schemes. Attempts were made to translate the large number of kinetic parameters generated into likelihoods of pellet breakage and rounding, with varying success. Model fitting and elucidation of the kinetic parameters were compounded due to the stochastic nature of the pellet breakage mechanism, which manifested in scatter for small data sets. These issues could possibly be mitigated by incorporating weighting functions for certain data and more rigorous fitting algorithms (e.g. [15]). An example of the former would be the incorporation of the coefficient of variation, σ/μ , for each experimental data point when calculating the coefficient of determination, R^2 , (viz)

$$(R^2)' = 1 - \sum \frac{(y_i - \hat{y}_i)^2}{(y_i - \bar{y})^2} \frac{1}{\left(\frac{\sigma_i}{\mu_i} + 1\right)} \tag{9}$$

Including this measure of spread for each point would improve the sensitivity to pellets that form fewer times during the process such as ones of length 5, flasks and bulbs.

The efficacy of applying any higher-order kinetic schemes would require further acquisition of properly characterised data sets, where pellet size and shape would be classified in an objective and unambiguous manner, as well as the incorporation of simultaneous breakage and rounding of pellets. The ability to analyse the dynamic behaviour of the pellets in terms of collisions between themselves and with the spheroniser surfaces would also be beneficial, along with a study of the different types of interactive energies involved.

Once achieved, model validation could be further explored

employing experimental data for longer spheronisation time periods and higher loadings, incorporating random starting lengths of extrudate, i.e. similar conditions to those used in industrial applications. Other parameters, such as spheroniser plate rotational speed and protuberance pattern, could also be addressed.

Rights retention statement

For the purposes of Open Access, the author has applied a Creative Commons Attribution (CC BY) licence to any Author Accepted Manuscript arising.

CRedit authorship contribution statement

J. Whelan-Smith: Writing – review & editing, Writing – original draft, Visualization, Validation, Methodology, Investigation, Formal analysis, Data curation, Conceptualization. **M.S. How:** Writing – review & editing, Visualization, Validation, Methodology, Investigation, Funding acquisition, Formal analysis, Data curation, Conceptualization. **S.L. Rough:** Writing - Original Draft, Writing - Review & Editing, Formal analysis, Conceptualization, Methodology, Project Administration. **L. Wang:** Writing – review & editing, Visualization, Validation, Methodology, Investigation, Funding acquisition, Formal analysis, Data

curation. **D.I. Wilson:** Writing – review & editing, Writing – original draft, Supervision, Resources, Project administration, Methodology, Funding acquisition, Formal analysis, Conceptualization.

Declaration of competing interest

None.

Data availability

The data reported here will be made available on the University of Cambridge Apollo repository at <https://doi.org/10.17863/CAM.105739>.

Acknowledgements

Ghaneassha Nadarajan contributed to the calculation of ideal pellet shape geometries in Fig. 2. Sabbatical leave funding for MSH from Universiti Putra Malaysia is gratefully acknowledged, as are discussions of parameter estimation methods with Prof. Raúl Conejeros, Escuela de Ingeniería Bioquímica, Pontificia Universidad Católica de Valparaíso (PUCV), Chile.

Appendix A. Appendix 1 2D Population balance model equations

The general kinetic scheme is

$$\frac{dN}{d\tau} = KN$$

where **N** is the column matrix of dimension 48 × 1

$$N = \begin{bmatrix} n_{6R} \\ n_{5R} \\ n_{4R} \\ n_{3R} \\ n_{2R} \\ \vdots \end{bmatrix} \quad (48 \times 1)$$

and **K** is the square matrix of coefficients, dimension 48 × 48

$$K = \begin{bmatrix} -(k_{6R,6H} + k_{6R,5R,1R} + k_{6R,4R,2R} + k_{6R,4R,3R}) & \dots & 0 \\ \vdots & \ddots & \vdots \\ 0 & \dots & 0 \end{bmatrix} \quad (48 \times 48)$$

giving.

Rods

$$\frac{dn_{6R}}{d\tau} = -n_{6R} (k_{6R,6H} + k_{6R,5R,1R} + k_{6R,4R,2R} + k_{6R,3R,3R})$$

$$\frac{dn_{5R}}{d\tau} = -n_{5R} (k_{5R,5H} + k_{5R,4R,1R} + k_{5R,3R,2R}) + n_{6R}k_{6R,5R,1R} + n_{6H}k_{6H,5H,1R} + n_{6F}k_{6F,5F,1R}$$

$$\frac{dn_{4R}}{d\tau} = -n_{4R} (k_{4R,4H} + k_{4R,3R,1R} + k_{4R,2R,2R}) + n_{6R}k_{6R,4R,2R} + n_{6H}k_{6H,4H,2R} + n_{5R}k_{5R,4R,1R} + n_{5H}k_{5H,4H,1R} + n_{6F}k_{6F,4F,2R} + n_{5F}k_{5F,4F,1R}$$

$$\frac{dn_{3R}}{d\tau} = -n_{3R} (k_{3R,3H} + k_{3R,2R,1R}) + 2n_{6R}k_{6R,3R,3R} + n_{6H}k_{6H,3H,3R} + n_{5R}k_{5R,3R,2R} + n_{5H}k_{5H,3H,2R} + n_{4R}k_{4R,3R,1R} + n_{4H}k_{4H,3H,1R} + n_{6F}k_{6F,3F,3R} + n_{5F}k_{5F,3F,2R} + n_{4F}k_{4F,3F,1R}$$

$$\frac{dn_{2R}}{d\tau} = -n_{2R} (k_{2R,2H} + k_{2R,1R,1R}) + n_{6R}k_{6R,4R,2R} + n_{6H}k_{6H,4H,2R} + n_{5R}k_{5R,3R,2R} + n_{5H}k_{5H,3H,2R} + 2n_{4R}k_{4R,2R,2R} + n_{4H}k_{4H,2H,2R} + n_{3R}k_{3R,2R,1R} + n_{3H}k_{3H,2H,1R} + n_{6F}k_{6F,4F,2R} + n_{5F}k_{5F,3F,2R} + n_{4F}k_{4F,2F,2R} + n_{3F}k_{3F,2F,1R}$$

$$\frac{dn_{1R}}{d\tau} = -n_{1R}k_{1R,1H} + n_{6R}k_{6R,5R,1R} + n_{6H}k_{6H,5H,1R} + n_{5R}k_{5R,4R,1R} + n_{5H}k_{5H,4H,1R} + n_{4R}k_{4R,3R,1R} + n_{4H}k_{4H,3H,1R} + n_{3R}k_{3R,2R,1R} + n_{3H}k_{3H,2H,1R} + 2n_{2R}k_{2R,1R,1R} + n_{2H}k_{2H,1H,1R} + n_{6F}k_{6F,5F,1R} + n_{5F}k_{5F,4F,1R} + n_{4F}k_{4F,3F,1R} + n_{3F}k_{3F,2F,1R} + n_{2F}k_{2F,1F,1R}$$

Half-cigars

$$\frac{dn_{6H}}{d\tau} = -n_{6H}(2k_{6H,5H,1R} + 2k_{6H,4H,2R} + k_{6H,3H,3R} + k_{6H,6C} + k_{6H,6F}) + n_{6R}k_{6R,6H}$$

$$\frac{dn_{5H}}{d\tau} = -n_{5H}(2k_{5H,4H,1R} + 2k_{5H,3H,2R} + k_{5H,5C} + k_{5H,5F}) + n_{6C}k_{6C,5H,1H} + n_{6H}k_{6H,5H,1R} + n_{6U}k_{6U,5F,1H} + n_{5R}k_{5R,5H}$$

$$\frac{dn_{4H}}{d\tau} = -n_{4H}(2k_{4H,3H,1R} + k_{4H,2H,2R} + k_{4H,4F} + k_{4H,4C}) + n_{6C}k_{6C,4H,2H} + n_{5C}k_{5C,4H,1H} + n_{6H}k_{6H,4H,2R} + n_{5H}k_{5H,4H,1R} + n_{6U}k_{6U,4F,2H} + n_{5U}k_{5U,4F,1H} + n_{4R}k_{4R,4H}$$

$$\frac{dn_{3H}}{d\tau} = -n_{3H}(2k_{3H,2H,1R} + k_{3H,3C} + k_{3H,3F}) + 2n_{6C}k_{6C,3H,3H} + n_{6H}k_{6H,3H,3R} + n_{5C}k_{5C,3H,2H} + n_{5H}k_{5H,3H,2R} + n_{4C}k_{4C,3H,1H} + n_{4H}k_{4H,3H,1R} + n_{6U}k_{6U,3F,3H} + n_{5U}k_{5U,3F,2H} + n_{4U}k_{4U,3F,1H} + n_{3R}k_{3R,3H}$$

$$\frac{dn_{2H}}{d\tau} = -n_{2H}(k_{2H,1H,1R} + k_{2H,2C} + k_{2H,2F}) + n_{6C}k_{6C,4H,2H} + n_{6H}k_{6H,4H,2R} + n_{5C}k_{5C,3H,2H} + n_{5H}k_{5H,3H,2R} + 2n_{4C}k_{4C,2H,2H} + n_{4H}k_{4H,2H,2R} + n_{3C}k_{3C,2H,1R} + n_{3H}k_{3H,2H,1R} + n_{6U}k_{6U,4F,2H} + n_{5U}k_{5U,3F,2H} + n_{4U}k_{4U,2F,2H} + n_{3U}k_{3U,2F,1H} + n_{2R}k_{2R,2H}$$

$$\frac{dn_{1H}}{d\tau} = -n_{1H}(k_{1H,1C} + k_{1H,1F}) + n_{6C}k_{6C,5H,1H} + n_{6H}k_{6H,5H,1R} + n_{5C}k_{5C,4H,1H} + n_{5H}k_{5H,4H,1R} + n_{4C}k_{4C,3H,1H} + n_{4H}k_{4H,3H,1R} + n_{3C}k_{3C,2H,1H} + n_{3H}k_{3H,2H,1R} + 2n_{2C}k_{2C,1H,1H} + n_{2H}k_{2H,1H,1R} + n_{6U}k_{6U,5F,1H} + n_{5U}k_{5U,4F,1H} + n_{4U}k_{4U,3F,1H} + n_{3U}k_{3U,2F,1H} + n_{2U}k_{2U,1F,1H} + n_{1R}k_{1R,1H}$$

Cigars

$$\frac{dn_{6c}}{d\tau} = -n_{6c}(k_{6c,5H,1H} + k_{6c,4H,2H} + k_{6c,3H,3H} + k_{6c,6U}) + n_{6H}k_{6H,6C}$$

$$\frac{dn_{5c}}{d\tau} = -n_{5c}(k_{5c,4H,1H} + k_{5c,3H,2H} + k_{5c,5U}) + n_{5H}k_{5H,5C}$$

$$\frac{dn_{4c}}{d\tau} = -n_{4c}(k_{4c,3H,1H} + k_{4c,2H,2H} + k_{4c,4U}) + n_{4H}k_{4H,4C}$$

$$\frac{dn_{3c}}{d\tau} = -n_{3c}(k_{3c,2H,1H} + k_{3c,3U}) + n_{3H}k_{3H,3C}$$

$$\frac{dn_{2c}}{d\tau} = -n_{2c}(k_{2c,1H,1H} + k_{2c,2U}) + n_{2H}k_{2H,2C}$$

$$\frac{dn_{1c}}{d\tau} = -n_{1c}k_{1c,1U} + n_{1H}k_{1H,1C}$$

Flasks

$$\frac{dn_{6F}}{d\tau} = -n_{6F}(2k_{6F,5F,1R} + 2k_{6F,4F,2R} + k_{6F,3F,3R} + k_{6F,6U}) + n_{6H}k_{6H,6F}$$

$$\frac{dn_{5F}}{d\tau} = -n_{5F}(2k_{5F,4F,1R} + 2k_{5F,3F,2R} + k_{5F,5U}) + n_{5H}k_{5H,5F} + n_{6F}k_{6F,5F,1R}$$

$$\frac{dn_{4F}}{d\tau} = -n_{4F}(2k_{4F,3F,1R} + 2k_{4F,2F,2R} + k_{4F,4U}) + n_{4H}k_{4H,4F} + n_{5F}k_{5F,4F,1R} + n_{6F}k_{6F,4F,2R}$$

$$\frac{dn_{3F}}{d\tau} = -n_{3F}(2k_{3F,2F,1R} + k_{3F,3U}) + n_{3H}k_{3H,3F} + n_{6F}k_{6F,3F,3R} + k_{5F,3F,2R} + n_{4F}k_{4F,3F,1R}$$

$$\frac{dn_{2F}}{d\tau} = -n_{2F}(k_{2F,1F,1R} + k_{2F,2U}) + n_{2H}k_{2H,2F} + n_{6F}k_{6F,4F,2R} + n_{5F}k_{5F,3F,2R} + n_{4F}k_{4F,2F,2R} + n_{3F}k_{3F,2F,1R}$$

$$\frac{dn_{1F}}{d\tau} = -n_{1F}k_{1F,1U} + n_{1H}k_{1H,1F} + n_{6F}k_{6F,5F,1R} + n_{5F}k_{5F,4F,1R} + n_{4F}k_{4F,3F,1R} + n_{3F}k_{3F,2F,1R} + n_{2F}k_{2F,1F,1R} + 2n_{2B}k_{2B,1F,1F}$$

Bulbs

$$\frac{dn_{6U}}{d\tau} = -n_{6U}(k_{6U,6D} + 2k_{6U,5F,1H} + 2k_{6U,4F,2H} + 2k_{6U,3F,3H}) + n_{6C}k_{6C,6U} + n_{6F}k_{6F,6U}$$

$$\frac{dn_{5U}}{d\tau} = -n_{5U}(k_{5U,5D} + 2k_{5U,4F,1H} + 2k_{5U,3F,2H}) + n_{5C}k_{5C,5U} + n_{5F}k_{5F,5U}$$

$$\frac{dn_{4U}}{d\tau} = -n_{4U}(k_{4U,4D} + 2k_{4U,3F,1H} + 2k_{4U,2F,2H}) + n_{4C}k_{4C,4U} + n_{4F}k_{4F,4U}$$

$$\frac{dn_{3U}}{d\tau} = -n_{3U}(k_{3U,3D} + 2k_{3U,2F,1H}) + n_{3c}k_{3C,3U} + n_{3F}k_{3F,3U}$$

$$\frac{dn_{2U}}{d\tau} = -n_{2U}(k_{2U,2D} + 2k_{2U,1F,1H}) + n_{2c}k_{2C,2U} + n_{2F}k_{2F,2U}$$

$$\frac{dn_{1U}}{d\tau} = -n_{1U}k_{1U,1D} + n_{1c}k_{1C,1U} + n_{1F}k_{1F,1U}$$

Dumbbells

$$\frac{dn_{6D}}{d\tau} = -n_{6D}(k_{6D,5F,1F} + k_{6D,4F,2F} + k_{6D,3F,3F}) + n_{6U}k_{6U,6D}$$

$$\frac{dn_{5D}}{d\tau} = -n_{5D}(k_{5D,4F,1F} + k_{5D,3F,2F}) + n_{5U}k_{5U,5D}$$

$$\frac{dn_{4D}}{d\tau} = -n_{4D}(k_{4D,3F,1F} + k_{4D,2F,2F}) + n_{4U}k_{4U,4D}$$

$$\frac{dn_{3D}}{d\tau} = -n_{3D}k_{3D,2F,1F} + n_{3U}k_{3U,3D}$$

$$\frac{dn_{2D}}{d\tau} = -n_{2D}(k_{2D,1F,1F} + k_{2D,2B}) + n_{2U}k_{2U,2D}$$

$$\frac{dn_{1D}}{d\tau} = -n_{1D}k_{1D,1B} + n_{1U}k_{1U,1D}$$

Bispheroids

$$\frac{dn_{6B}}{d\tau} = \frac{dn_{5B}}{d\tau} = \frac{dn_{4B}}{d\tau} = \frac{dn_{3B}}{d\tau} = 0$$

$$\frac{dn_{2B}}{d\tau} = -n_{2B}k_{2B,1F,1F} + n_{2D}k_{2D,2B}$$

$$\frac{dn_{1B}}{d\tau} = -n_{1B}k_{1B,1S} + n_{1D}k_{1D,1B}$$

Spheroids

$$\frac{dn_{6S}}{d\tau} = \frac{dn_{5S}}{d\tau} = \frac{dn_{4S}}{d\tau} = \frac{dn_{3S}}{d\tau} = \frac{dn_{2S}}{d\tau} = 0$$

$$\frac{dn_{1S}}{d\tau} = n_{1B}k_{1B,1S}$$

Appendix B. Supplementary data

Supplementary data to this article can be found online at <https://doi.org/10.1016/j.powtec.2024.119465>.

References

- [1] C. Vervaet, L. Baert, J.P. Remon, Extrusion-spheronisation: a literature review, *Int. J. Pharm.* 116 (2) (1995) 131–146.
- [2] D.I. Wilson, S.L. Rough, Extrusion-Spheronisation, in: A.D. Salman, M.J. Hounslow (Eds.), *Granulation*, Elsevier, Amsterdam, 2007, pp. 189–210.
- [3] M. Koester, M. Thommes, Analysis of particle kinematics in spheronisation via particle image velocimetry, *Eur. J. Pharm. Biopharm.* 83 (2013) 307–314.
- [4] D. Weis, P. Grohn, M. Evers, M. Thommes, E. Garcia, S. Antonyuk, Implementation of formation mechanisms in DEM simulation of the spheronization process of pharmaceutical pellets, *Powder Tech* 378 (2021) 667–679.
- [5] C.L.S. Lau, Q. Yu, V.Y. Lister, S.L. Rough, D.I. Wilson, M. Zhang, The evolution of pellet size and shape during spheronisation of an extruded microcrystalline cellulose paste, *Chem. Eng. Res. Des.* 92 (11) (2014) 2413–2424.
- [6] M.P. Bryan, L.N. Atherton, S. Duffield, S.L. Rough, D.I. Wilson, Stages in spheronisation: evolution of pellet size and shape during spheronisation of microcrystalline cellulose-based paste extrudates, *Powder Tech.* 270 (2015) 163–175.
- [7] C.I. Sinka, A first order numerical study of the spheronisation process, *Powder Tech.* 206 (2011) 195–200.
- [8] C.I. Sinka, A model for the deformation of an ellipsoid subject to a large number of successive impacts with special reference to spheronisation, *Powder Tech.* 270 (2015) 592–598.
- [9] Y. Guo, C. Wassgren, B. Hancock, W. Ketterhagen, J. Curtis, Predicting breakage of high aspect ratio particles in an agitated bed using the discrete element method, *Chem. Eng. Sci.* 158 (2017) (2017) 314–327.
- [10] J. Parkin, K.S. Widjaja, M.P. Bryan, S.L. Rough, D.I. Wilson, A dimensional analysis of spheronisation of cylindrical extrudates, *Powder Tech.* 298 (2016) 73–83.
- [11] M. Evers, D. Weis, A. Antonyuk, M. Thommes, Scale-up of the rounding process in pelletization by extrusion-spheronization, *Pharm. Dev. Tech.* 24 (8) (2019) 1014–1102.
- [12] L. Wang, C.W. Lim, G.Z.L. Ng, S.L. Rough, D.I. Wilson, Modeling the breakage stage in spheronization of cylindrical paste extrudates, *AIChEJ* 67 (6) (2021) e17247.
- [13] M. Zhang, Y. Li, J.F. Xing, S.L. Rough, D.I. Wilson, Influence of plate surface protuberances on the production of pharmaceutical paste pellets by extrusion-spheronisation, *Chem. Eng. Res. Des.* 109 (2016) 97–107.
- [14] X. Ying, An overview of overfitting and its solutions, *J. Phys. Conf. Ser.* 1168 (2019) 022022.
- [15] K. Egan, W. Li, R. Carvalho, Automatically discovering ordinary differential equations from data with sparse regression, *Commun. Phys.* 7 (2024) 20, <https://doi.org/10.1038/s42005-023-01516-2>.